The Astrophysical Journal Letters, 971:L21 (10pp), 2024 August 10 https://doi.org/10.3847/2041-8213/ad67e5

First Detection of X-Ray Polarization in Galactic Ultraluminous X-Ray Pulsar Swift J0243.6+6124 with IXPE

Seshadri Majumder[1], Rwitika Chatterjee[2], Kiran M. Jayasurya[2], Santabrata Das[1], and Anuj Nandi[2]
[1] Indian Institute of Technology Guwahati, Guwahati, 781039, India
[2] Space Astronomy Group, ISITE Campus, U. R. Rao Satellite Centre, Outer Ring Road, Marathahalli, Bangalore, 560037, India
Received 2024 February 19; revised 2024 July 10; accepted 2024 July 23; published 2024 August 7

Abstract

We report the results of first ever spectropolarimetric analyses of the Galactic ultraluminous X-ray pulsar Swift J0243.6+6124 during the 2023 outburst using quasi-simultaneous IXPE, NICER, and NuSTAR observations. A pulsation of period ∼9.79 s is detected in IXPE and NuSTAR observations with pulse fractions (PFs) ∼18% (2–8 keV) and ∼28% (3–78 keV), respectively. Energy-dependent study of the pulse profiles with NuSTAR indicates an increase in PF from ∼27% (3–10 keV) to ∼50% (40–78 keV). Further, epoch-dependent polarimetric measurements during the decay phase of the outburst confirm the detection of significant polarization, with the polarization degree (PD) and polarization angle ranging between ∼2%–3.1% and ∼8°.6–10°.8, respectively, in the 2–8 keV energy range. We also observe that the PD increases up to ∼4.8% at higher energies ($\gtrsim$5 keV) with dominating `bbodyrad` flux contribution ($1.5 \lesssim F_{\rm BB}/F_{\rm PL} \lesssim 3.4$) in the IXPE spectra. The phase-resolved polarimetric study yields PD as ∼1.7%–3.1% suggesting a marginal correlation with the pulse profiles. Moreover, the broadband (0.6–70 keV) energy spectrum of combined NICER and NuSTAR observations is well described by the combination of `bbodyrad` and `cutoffpl` components with seed photon temperature ($kT_{\rm bb}$) $\sim 0.86 \pm 0.03$ keV and photon index (Γ) $\sim 0.98 \pm 0.01$. With the above findings, we infer that the observed "low" PD in Swift J0243.6+6124 is attributed possibly due to the "vacuum resonance" effect between the overheated and relatively cooler regions of the neutron star boundary layer.

Unified Astronomy Thesaurus concepts: Magnetic fields (994); Neutron stars (1108); Accretion (14); X-ray binary stars (1811)

1. Introduction

Ultraluminous X-ray pulsar sources (ULXPs) are bright pointlike off-nuclear objects containing neutron stars with isotropic luminosity ($\sim 10^{39-41}$ erg s^{-1}) exceeding the Eddington limit (see Feng & Soria 2011; King et al. 2023 for review). Alongside the black hole candidates (Atapin et al. 2019; Majumder et al. 2023), the detection of 1.4 s X-ray pulsation in M82 X−2 (Bachetti et al. 2014) opened up a completely new window to understand the characteristics of ultraluminous X-ray sources. Meanwhile, nine confirmed ULXPs have been reported with the detection of X-ray pulsation (King et al. 2023, and references therein) to date.

Admittedly, the accretion onto the X-ray pulsars (XRPs) is regulated by strong magnetic fields ($\sim 10^{12-13}$ G). The accreted matter is channeled along the magnetic field lines at the magnetospheric radius and generates hotspots near the magnetic poles of the neutron star (NS) that radiates pulsed emission in X-rays being misaligned with the spin axis (see Mushtukov & Tsygankov 2022 for a recent review). It is believed that at higher mass accretion rates, the hotspots turn into vertically extended accretion columns above the NS surface (Basko & Sunyaev 1976; Mushtukov et al. 2015). However, the relative contribution in total emission from the accretion column, depending on the disk truncation radius, is found to play a vital role for the irregular pulsations detected in most of the known ULXPs (Walton et al. 2018). Indeed, ULXP spectra are empirically well described by blackbody-like emissions and power-law profiles with high energy cut-off.

The Imaging X-ray Polarimetry Explorer (IXPE; Weisskopf et al. 2022) provides a unique opportunity to probe the X-ray polarization of XRPs. So far, the detection of phase-averaged/resolved polarized emission in a handful of XRPs, such as Her X−1 (∼10%; Doroshenko et al. 2022), Cen X−3 (∼5.8%; Tsygankov et al. 2022), 4U 1626 − 67 (∼4.8%; Marshall et al. 2022), Vela X−1 (∼2.3%; Forsblom et al. 2023), GRO J1008 − 57 (∼15%; Tsygankov et al. 2023), EXO 2030 + 375 (∼3%; Malacaria et al. 2023), X Persei (∼20%; Mushtukov et al. 2023), and GX 301 − 2 (∼3%–10%; Suleimanov et al. 2023) is confirmed with IXPE. If not all, most of the sources show a "low" polarization degree (PD) compared to the predictions from the existing models (Meszaros et al. 1988; Caiazzo & Heyl 2021a, 2021b), and its cause remains an open question to date.

Indeed, most of the aforementioned models were developed neglecting the possible effects of specific temperature profiles at the NS surface. It is important to note that due to accretion, the overheated upper boundary layer of the NS surface can significantly alter the properties of polarized emission (Tsygankov et al. 2022). In addition, the complex magnetic field geometry perhaps causes the mixing of emissions from different parts of the NS surface, which could possibly result in "low" PD in EXO 2030 + 375 (Malacaria et al. 2023). Furthermore, the scattering and reprocessing of X-ray emissions in the surrounding stellar wind of the companion can marginally depolarize the intrinsic emission up to 10%–15% (Suleimanov et al. 2023). Notably, significant phase-dependent polarization properties are often observed in XRPs despite the low phase-averaged measurements. For example,

Table 1
Details of Quasi-simultaneous IXPE, NICER, and NuSTAR Observations of Swift J0243.6+6124

Epoch	Mission	Date	ObsID	MJD_{start}	MJD_{stop}	Exposure (ks)
NI0	NICER	2023-06-27	6050390237	60122.05	60122.96	4
NU0	NuSTAR	2023-06-27	90901321002	60122.53	60123.08	12
IX1	IXPE	2023-07-20	02250799	60145.63	60148.65	167
NI1	NICER	2023-07-20	6050390252	60145.28	60145.93	1.6
...	NICER	2023-07-21	6050390253	60146.51	60146.77	0.8
...	NICER	2023-07-22	6050390254	60147.02	60147.80	1.9
IX2	IXPE	2023-08-09	02250799	60165.99	60167.37	77
NI2	NICER	2023-08-12	6050390255	60168.27	60168.98	1.7
IX3	IXPE	2023-08-23	02250799	60179.42	60181.81	131
NI3	NICER	2023-08-23	6050390265	60179.68	60179.69	0.7

GX 301 − 2 exhibits a polarization of ∼3%–10% over different pulse phases, whereas the phase-averaged estimate results in a null detection (Suleimanov et al. 2023). Similar findings are also observed in GRO J1008 − 57 (Tsygankov et al. 2023) and Vela X−1 (Forsblom et al. 2023).

In this work, we study the polarization properties of the transient XRP Swift J0243.6+6124 for the first time, using IXPE observations of this source. The source, with a Be-star binary companion (Reig et al. 2020), was discovered (Kennea et al. 2017) during its giant outburst in 2017 by Swift/Burst Alert Telescope (BAT) with a peak flux of ∼8.2 Crab and pulse period of ∼9.86 s (Kennea et al. 2017). With the measured source distance of 6.8 kpc (Bailer-Jones et al. 2018), the peak luminosity of the source Swift J0243.6+6124, classified as the first Galactic ULXP (Tsygankov et al. 2018), exceeds the Eddington limit of an NS system.

In this Letter, we present the results of in-depth phase-averaged/resolved spectropolarimetric analyses of Swift J0243.6+6124 with IXPE in the 2–8 keV energy range. In addition, we also use quasi-simultaneous NICER and NuSTAR observations to study the broadband (0.6–70 keV) spectral distribution of the source.

The Letter is organized as follows: In Section 2, we mention the observation details along with the data reduction procedures of each instrument. In Section 3, we present the results obtained from the spectropolarimetric studies. Finally, we summarize our findings and conclude in Section 4.

2. Observation and Data Reduction

IXPE observed Swift J0243.6+6124 three times between 2023 July 20 and 2023 August 25 for a total exposure of about ∼375 ks during the decay phase of its 2023 outburst. The entire observation is segmented into three epochs of ∼167 ks (IX1, MJD_{start} 60145.63), ∼77 ks (IX2, MJD_{start} 60165.99), and ∼131 ks (IX3, MJD_{start} 60179.42) exposures, respectively. We make use of cleaned and calibrated level-2 event files from the three detector units (DUs) of IXPE (2–8 keV). The data analysis is carried out using `IXPEOBSSIMv30.5.0` software (Baldini et al. 2022) following standard procedures mentioned in Kislat et al. (2015), Strohmayer (2017), Kushwaha et al. (2023), and Majumder et al. (2024). The source and background regions are considered as the 60″ circular region at the source coordinate and the annular region between 180″ and 240″ radii with the same center, respectively (see also Jayasurya et al. 2023; Majumder et al. 2024). Further, the `XPSELECT` task is used to extract the source and background events from the selected regions. We use `XPBIN` task with various algorithms such as `PCUBE`, `PHA1`, `PHA1Q`, and `PHA1U` to generate necessary data products for model-independent (Kislat et al. 2015) and spectropolarimetric (Strohmayer 2017) studies. Finally, the `XPPHASE` task is used to assign phase to barycenter-corrected[3] IXPE events lists for phase-resolved polarimetric studies.

Swift J0243.6+6124 is also observed by NICER and NuSTAR during the 2023 outburst. In this work, we analyze quasi-simultaneous NICER (∼4 ks) and NuSTAR (∼12 ks) observations (hereafter NI0 and NU0) carried out on 2023 June 27. Additionally, we consider multiple NICER observations (hereafter NI1, NI2, and NI3) which are quasi-simultaneous with the three IXPE epochs (IX1, IX2, and IX3), respectively. The details of all the multimission observations along with their exposures used in this work are tabulated in Table 1. The data are processed using standard analysis software `NICERDASv11a` and `nupipelinev0.4.9` for NICER and NuSTAR, respectively, integrated in `HEASOFT V6.32.1`.[4] We use appropriate calibration databases while analyzing data.

3. Analysis and Results

3.1. Outburst Profile

Swift J0243.6+6124 has been monitored by MAXI/Gas Slit Camera (GSC; 2–20 keV) and Swift/BAT (15–50 keV) almost on a daily basis since the trigger of its giant outburst in 2017. We present the complete coverage of the source with different instruments since its detection in panel (a) of Figure 1. The recent outburst in 2023 covered by both Swift/BAT and MAXI/GSC is shown in panels (b) and (c) of Figure 1, respectively. We observe an almost similar profile of the rise and decay phases of the outburst with peak MAXI/GSC and Swift/BAT flux of about 2.27 counts $cm^{-2}\,s^{-1}$ (597 mCrab) and ∼0.26 counts $cm^{-2}\,s^{-1}$ (1.2 Crab) in the 2–20 keV and 15–50 keV energy ranges, respectively. The background-subtracted IXPE light curves of 1000 s bin combining all three DUs (2–8 keV) during epochs IX1 (∼973 mCrab), IX2 (∼843 mCrab), and IX3 (∼314 mCrab) are shown in panel (b) using blue open circles along with the entire observation period in gray shade. The quasi-simultaneous NICER and NuSTAR observations over different epochs are marked with vertical dashed lines. We observe that the average IXPE count rate gradually decreases as 29.46 cts s^{-1} (IX1), 16.47 cts s^{-1} (IX2), and 6.55 cts s^{-1} (IX3) during the decay phase of the outburst.

[3] https://heasarc.gsfc.nasa.gov/ftools/caldb/help/barycorr.html
[4] https://heasarc.gsfc.nasa.gov/docs/software/heasoft

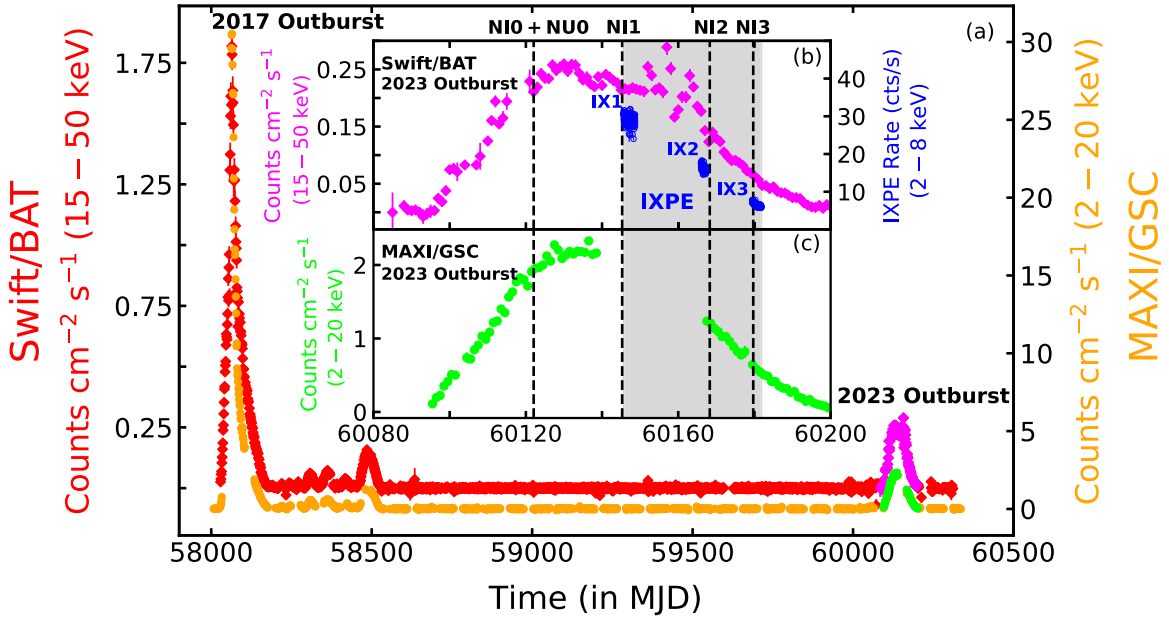

Figure 1. Panel (a): 1 day binned *MAXI/GSC* (orange) and Swift/BAT (red) light curves of Swift J0243.6+6124 since its discovery (2017 October) in the 2–20 keV and 15–50 keV energy bands. Panels (b) and (c): zoomed view of the 2023 outburst observed with Swift/BAT (magenta) and MAXI/GSC (green). Epochs of NICER and NuSTAR observations are marked with vertical lines. The gray patch indicates the duration of IXPE observations, and blue circles denote the corresponding IXPE count rates of 1000 s bin combining all three DUs (2–8 keV).

3.2. Phase-averaged Polarimetric Measurements

3.2.1. Model-independent PCUBE Results

For model-independent analysis, we use the PCUBE algorithm to estimate normalized Stokes parameters, polarization angle (PA), PD, and minimum detectable polarization at 99% confidence (MDP_{99}%) following Majumder et al. (2024), and references therein. Considering all events from three DUs of IXPE, we measure the polarization parameters during epoch IX1 as $PD = 2.0\% \pm 0.2\%$ ($>8\sigma$), $PA = 10.^{\circ}8 \pm 3.^{\circ}3$ with $MDP_{99} = 0.7\%$ in the 2–8 keV energy band. We also detect significant polarization ($PD > MDP_{99}$, $\sigma > 3$) during epochs IX2 and IX3, respectively. We observe that PD increases to $\sim 3.1\% \pm 0.5\%$ ($>6\sigma$) in epoch IX2, which subsequently decreases to $2.4\% \pm 0.5\%$ ($>3\sigma$) in epoch IX3. Note that the constrained PA remains $0.^{\circ}7 \pm 4.^{\circ}2$ in epoch IX2 and becomes $8.^{\circ}9 \pm 6.^{\circ}4$ during epoch IX3. Following Krawczynski et al. (2022), we estimate the significance of the PD variation in different epochs considering the χ^2 statistics of 2 degrees of freedom. Here, we consider the null hypothesis as $PD = 2.2\% \pm 0.2\%$, obtained from the data combining all the epochs. With this, we find that the change in PD over the epochs is significant at a 92% confidence level, indicating a marginal variation. In Figure 3(a), we present the corresponding variation of the normalized Stokes parameters (Q/I and U/I) over different epochs along with 1σ contours in Q-U space. Furthermore, we estimate the significance of the variations of normalized Stokes parameters (Q/I and U/I) over different epochs against the respective averaged-out values, considering $2(n-1)$ degrees of freedom, n being the number of Q/I–U/I pairs. We find that the variation in Q/I and U/I over three IXPE epochs is significant at a 97.1% confidence within the 2–8 keV energy range, which is higher than the obtained significance (92%) of the corresponding variation in PD. This is expected because of the independent and Gaussian nature of the error distributions associated with the Stokes parameters.

Further, to infer the energy-dependent polarimetric properties, we estimate polarization parameters in different energy bands, namely 2–3.5, 3.5–5, 5–6.5, and 6.5–8 keV, respectively. We observe an increase of PD from ∼1.4% (2–3.5 keV) to a maximum of ∼3.3% (5–6.5 keV) with a null-detection in the 6.5–8 keV energy band during epoch IX1. We estimate the significance of the energy-dependent PD variation in each epoch following the approach discussed above. In doing so, we consider the χ^2 statistics of 3 degrees of freedom (corresponding to four energy bins) and compute the significance against the PD in the 2–8 keV energy band (see Table 2) of the respective epochs. We find that the increase of PD with energy is significant at 98.8% (IX1), 93.2% (IX2), and 75.5% (IX3) confidence levels for the individual epochs. Based on these results, we indicate that the PD moderately increases with energy for IX1, whereas marginal variation with energy is observed for IX2 and IX3, respectively. However, the energy dependence of PA is found to be insignificant. In Figure 2(a), we present 2σ confidence contours of PD and PA in different energy ranges for epoch IX1. The obtained energy-dependent behavior of PD and PA at different epochs (IX1 and IX2) is shown in Figure 2(b). The estimated parameters for all epochs are listed in Table 2. Note that the estimated PD for some of the energy bands (see Figure 2(b)) remains very close to or below the MDP_{99}% level due to poor statistics obtained in the respective energy bands, which requires careful interpretation of the obtained results. Furthermore, in Figure 3(b), we show the variation of normalized Stokes parameters (Q/I and U/I) obtained for epoch IX1 over different energy bands with 1σ contours. As before, a measurement of the significance associated with the variation in Stokes parameter space results in a marginally improved statistical interpretation of the energy variation of polarimetric parameters, significant at 97.6% (IX1),

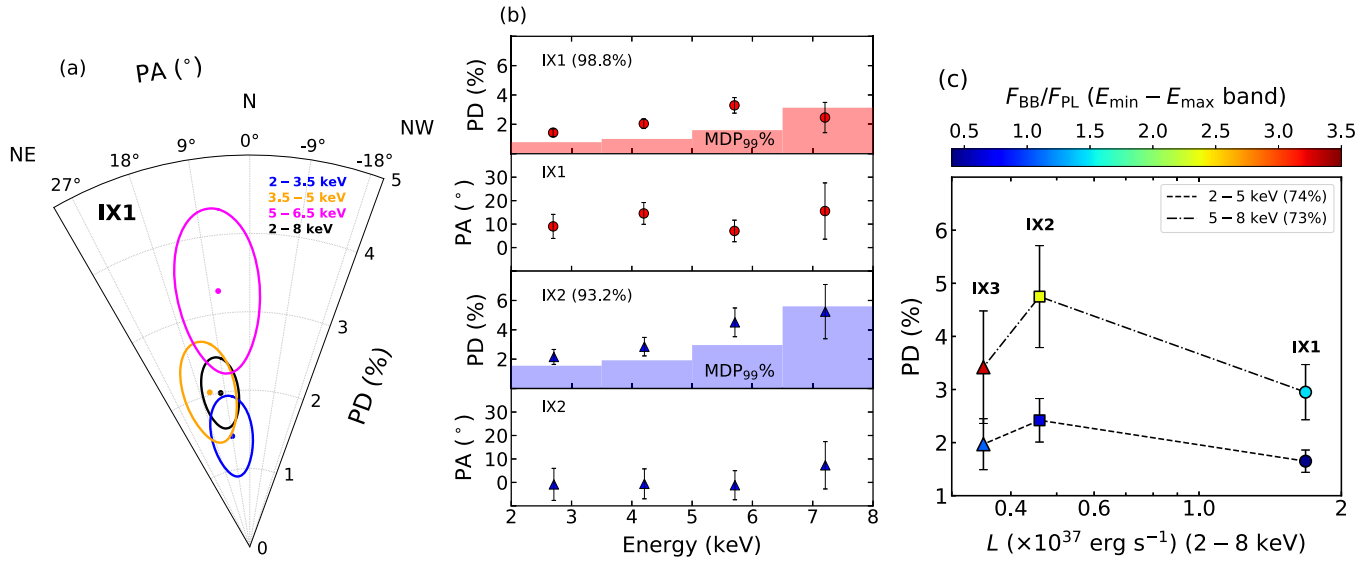

Figure 2. Left: confidence contours (2σ) of PD and PA obtained in epoch IX1 are shown with different colors for different energy bands. Middle: variations of PD and PA with energy for epoch IX1 (MJD_{start} 60145.63) and IX2 (MJD_{start} 60165.99). Histograms denote MDP_{99}%, and confidence levels (%) for PD variations with energy are mentioned in the legend. Right: correlation of PD (model-independent) with luminosity and flux ratio (F_{BB}/F_{PL}) from spectropolarimetric modeling of IXPE data. PD variations are significant at 74% and 73% in the respective energy bands.

Table 2
Results from Model-independent Polarimetric Analyses in Different Energy Bands for Three Epochs (IX1, IX2, and IX3)

Epoch (Exposure)	Pulse Period (s)	Parameters	2–3.5 (keV)	3.5–5 (keV)	5–6.5 (keV)	6.5–8 (keV)	2–8 (keV)	2–5 (keV)	5–8 (keV)
IX1	9.79301(1)	PD (%)	1.4 ± 0.3	2.0 ± 0.3	3.3 ± 0.5	2.5 ± 1.0	2.0 ± 0.2	1.7 ± 0.2	3.0 ± 0.5
(∼167 ks)		PA (deg)	9.0 ± 5.1	14.6 ± 4.6	7.1 ± 4.6	15.6 ± 12.0	10.8 ± 3.3	11.5 ± 3.6	9.7 ± 5.1
		Q/I (%)	1.4 ± 0.3	1.8 ± 0.3	3.2 ± 0.5	2.1 ± 1.0	1.9 ± 0.2	1.5 ± 0.2	2.8 ± 0.5
		U/I (%)	0.4 ± 0.3	1.0 ± 0.3	0.8 ± 0.5	1.3 ± 1.0	0.7 ± 0.2	0.6 ± 0.2	1.0 ± 0.5
		MDP_{99} (%)	0.8	1.0	1.6	3.1	0.7	0.6	1.6
		SIGNIF (σ)	5.1	5.7	5.8	1.6	8.7	7.6	5.2
IX2	9.79204(2)	PD (%)	2.2 ± 0.5	2.9 ± 0.6	4.5 ± 1.0	5.2 ± 1.9	3.1 ± 0.5	2.4 ± 0.4	4.8 ± 1.0
(∼77 ks)		PA (deg)	-0.8 ± 6.8	-0.6 ± 6.4	-1.2 ± 6.2	7.3 ± 10.1	0.7 ± 4.2	-0.7 ± 4.8	2.5 ± 5.8
		Q/I (%)	2.2 ± 0.5	2.9 ± 0.6	4.5 ± 1.0	5.1 ± 1.9	3.1 ± 0.5	2.4 ± 0.4	4.7 ± 1.0
		U/I (%)	-0.1 ± 0.5	-0.1 ± 0.6	-0.2 ± 1.0	1.3 ± 1.9	0.1 ± 0.5	-0.1 ± 0.4	0.4 ± 1.0
		MDP_{99} (%)	1.6	1.9	3.0	5.6	1.4	1.2	2.9
		SIGNIF(σ)	3.6	3.9	4.1	2.1	6.5	5.50	4.43
IX3	9.79371(3)	PD (%)	1.4 ± 0.6	2.8 ± 0.7	3.6 ± 1.1	3.5 ± 2.0	2.4 ± 0.5	2.0 ± 0.5	3.4 ± 1.1
(∼131 ks)		PA (deg)	-2.8 ± 12.6	5.1 ± 7.5	10.0 ± 8.7	26.1 ± 16.5	8.6 ± 6.4	1.8 ± 7.0	16.2 ± 8.9
		Q/I (%)	1.4 ± 0.6	2.7 ± 0.7	3.4 ± 1.1	2.2 ± 2.0	2.3 ± 0.5	2.0 ± 0.5	2.9 ± 1.1
		U/I (%)	-0.1 ± 0.6	0.5 ± 0.7	1.2 ± 1.1	2.8 ± 2.0	0.7 ± 0.5	0.1 ± 0.5	1.8 ± 1.1
		MDP_{99} (%)	1.9	2.2	3.3	6.2	1.6	1.5	3.2
		SIGNIF (σ)	1.4	3.2	2.6	0.8	3.9	3.5	2.5

Note. Here, PD, PA, Q/I, U/I, MDP_{99}, and SIGNIF denote polarization degree, angle of polarization, normalized Q-Stokes parameter, normalized U-Stokes parameter, minimum detectable polarization at 99% confidence, and detection significance, respectively.

95.4% (IX2), and 84.4% (IX3) confidence levels in different epochs.

3.2.2. Model-dependent Spectropolarimetric Results

We simultaneously fit the I, Q, and U Stokes spectra from all DUs (2–8 keV) within `XPSEC`, considering a standard model combination, `const*Tbabs*polconst*(Gaussian +bbodyrad+cutoffpl)`, for spectropolarimetric modeling. Here, `polconst` represents a constant polarization model with PD and PA as the model parameters. We obtain the best fit with $\chi^2_{red} = 1.2$ resulting in PD = 1.9% ± 0.2% and PA = $10.^{\circ}3 \pm 2.^{\circ}9$ in epoch IX1. Further, the seed photon temperature (kT_{bb}) and photon index (Γ) are obtained as $2.03^{+0.05}_{-0.04}$ keV and 1.64 ± 0.03, respectively, during epoch IX1.

Next, we replace `polconst` with the energy-dependent polarization model `polpow` that fits Q and U Stokes spectra considering $PD(E)=A_{norm} \times E^{-A_{index}}$ and $PA(E)=\psi_{norm} \times E^{-\psi_{index}}$. We find that the model fitted ψ_{index} remains consistent with zero within 1σ. Hence, we freeze it to zero while modeling. This yields the best-fitted polarization parameters of epoch IX1 with $A_{index} = -0.98 \pm 0.3$, $A_{norm} = 0.0051^{+0.0028}_{-0.0019}$, and $\psi_{norm} = 10.^{\circ}5 \pm 2.^{\circ}7$ with $\chi^2_{red} = 1.2$. It is worth mentioning that A_{index} is consistent with zero at 3σ level, suggesting a marginal energy variation ($<3\sigma$). This is consistent with the

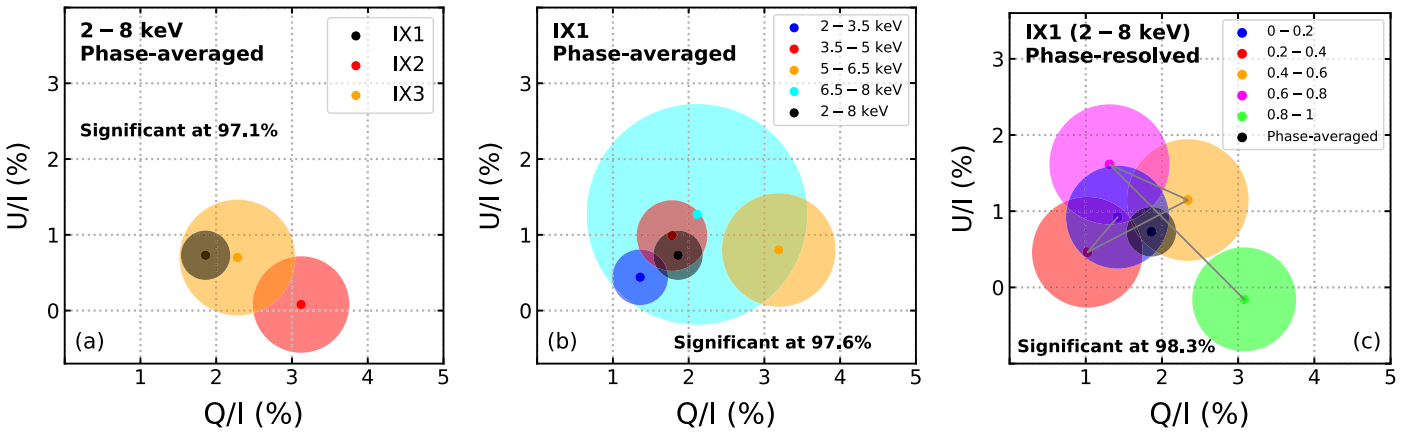

Figure 3. Normalized stokes parameters (Q/I and U/I) obtained with PCUBE analyses for (a) different epochs (2–8 keV), (b) energy bands (epoch IX1), and (c) phase bins (epoch IX1 in 2–8 keV). The radii of colored circles represent 1σ uncertainty values corresponding to 2 degrees of freedom. See the main text for details.

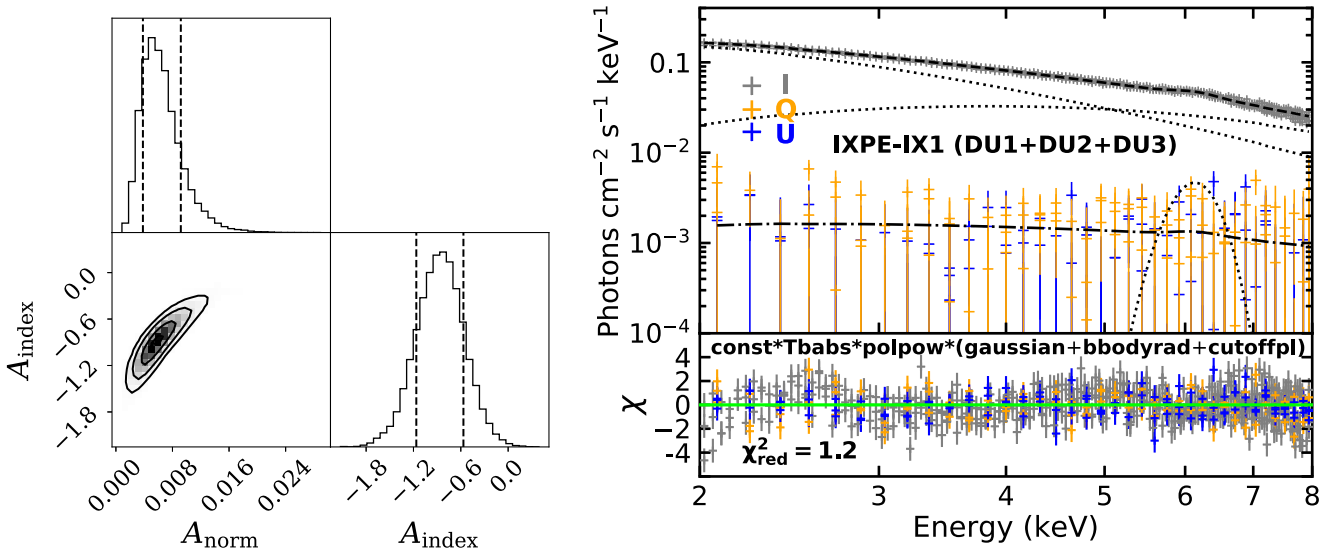

Figure 4. Left: corner plot shows the covariance between best-fitted $A_{\rm index}$ and $A_{\rm norm}$ parameters of the polpow model in the 2–8 keV energy band, obtained using the MCMC method. The contours represent the 1σ, 2σ, and 3σ confidence ranges, respectively. Right: best-fitted I, Q, and U Stokes spectra of IXPE combining all DUs in the 2–8 keV energy range (top panel) and corresponding residual variation (bottom panel). See the main text for details.

energy-dependent results significant at 2.5σ (IX1), obtained from the model-independent approach. Moreover, to explore the covariance between $A_{\rm index}$ and $A_{\rm norm}$, we conduct a Markov Chain Monte Carlo (MCMC) simulation in XSPEC using the Goodman–Weare algorithm (Goodman & Weare 2010) with a chain length of 200,000. The obtained results are presented in the left panel of Figure 4, where strong covariance between $A_{\rm index}$ and $A_{\rm norm}$ is observed in their respective error regions, which limits the ability to independently constrain one parameter from the other. Next, integrating PD(E) and PA(E) with best-fitted model parameters over 2–8 keV, we obtain PD and PA as $2.3\% \pm 0.2\%$ and $10\overset{\circ}{.}5 \pm 2\overset{\circ}{.}7$, respectively. Similar model combinations are also found to provide the best fit in epochs IX2 (PD $= 3.6\% \pm 0.2\%$, PA $= 0\overset{\circ}{.}8 \pm 3\overset{\circ}{.}5$) and IX3 (PD $= 3.0\% \pm 0.3\%$, PA $= 7\overset{\circ}{.}5 \pm 4\overset{\circ}{.}9$). In particular, a fit with the pollin model (linearly varying polarization with energy) yields the parameters A1 and Aslope being consistent with zero at the 1σ level and hence fails to constrain the polarization parameters PD and PA.

Further, we adopt the model combination const*Tbabs*(polconst*Gaussian +polconst*bbodyrad+polconst*cutoffpl) to estimate the polarization level of each model component. We observe that the best fit yields PD $= 4.7\% \pm 1.3\%$ and PA $= 11\overset{\circ}{.}1 \pm 8\overset{\circ}{.}4$ with $\chi^2_{\rm red} = 1.2$ associated with the bbodyrad component, whereas the Gaussian and cutoffpl components remain unpolarized, with PD and PA unconstrained at 1σ. All the model-fitted and estimated parameters obtained from the spectropolarimetric modeling are tabulated in Table 3. The best-fitted I, Q, and U Stokes spectra of IXPE in the 2–8 keV energy range and the corresponding residual variations are depicted in the right panel of Figure 4. In the figure, the dotted curves represent the model components (bbodyrad, cutoffpl, and Gaussian) obtained from the best fit of the I Stokes spectra. The dotted–dashed curve corresponds to the best-fitted model of the Q and U Stokes spectra, while the dashed curve depicts the best-fitted effective model for the I Stokes spectra.

Furthermore, we attempt to deduce the correlation between PD (model-independent), luminosity, and the ratio of bbodyrad to cutoffpl fluxes ($F_{\rm BB}/F_{\rm PL}$) obtained with cflux from the modeling of IXPE spectra (2–8 keV). In Figure 2(c), we present the variation of PD (2–5 and 5–8 keV) with luminosity (2–8 keV). The color code denotes the flux ratio ($F_{\rm BB}/F_{\rm PL}$) computed using the polpow component

Table 3
Results from Spectropolarimetric Analysis of the IXPE Stokes Spectra for Different Epochs in the 2–8 keV Energy Range

Component	Epoch	$A_{\rm norm}$	$A_{\rm index}$	$\psi_{\rm norm}$ (deg)	$kT_{\rm bb}$ (keV)	Γ	$\chi^2_{\rm red}$	PD (%)	PA (deg)	$F_{\rm BB}/F_{\rm PL}$ (2–8 keV)	$L_{\rm IXPE}$ (2–8 keV) ($\times 10^{37}$ erg s^{-1})	$L_{\rm NICER}$ (0.6–11 keV) ($\times 10^{37}$ erg s^{-1})
`polconst`	IX1	⋯	⋯	⋯	$2.03^{+0.05}_{-0.04}$	$1.64^{+0.03}_{-0.03}$	1.20	1.86 ± 0.19	10.28 ± 2.86	⋯	⋯	⋯
	IX2	⋯	⋯	⋯	$2.12^{+0.09}_{-0.08}$	$1.66^{+0.07}_{-0.07}$	1.15	2.81 ± 0.36	0.70 ± 3.68	⋯	⋯	⋯
	IX3	⋯	⋯	⋯	$2.03^{+0.08}_{-0.07}$	$1.46^{+0.13}_{-0.13}$	1.02	2.44 ± 0.42	5.93 ± 4.97	⋯	⋯	⋯
`polpow`[a]	IX1	$0.0051^{+0.0028}_{-0.0019}$	$-0.98^{+0.30}_{-0.30}$	10.46 ± 2.74	$2.03^{+0.05}_{-0.04}$	$1.64^{+0.03}_{-0.03}$	1.20	2.30 ± 0.23	10.46 ± 2.74	0.71	1.68 ± 0.02	8.58 ± 0.02
	IX2	$0.0075^{+0.0062}_{-0.0036}$	$-0.98^{+0.41}_{-0.42}$	0.77 ± 3.53	$2.12^{+0.09}_{-0.08}$	$1.66^{+0.07}_{-0.07}$	1.14	3.63 ± 0.17	0.77 ± 3.53	1.10	0.46 ± 0.01	4.37 ± 0.02
	IX3	$0.0084^{+0.0056}_{-0.0049}$	$-0.79^{+0.54}_{-0.56}$	7.46 ± 4.93	$2.03^{+0.08}_{-0.07}$	$1.46^{+0.13}_{-0.13}$	1.02	2.96 ± 0.31	7.46 ± 4.93	1.73	0.35 ± 0.01	2.21 ± 0.01

Note.
[a] $\psi_{\rm index}$ of `polpow` is consistent with zero at 1σ. Hence, it is frozen to zero while obtaining best-fit parameters.

in the respective energy bands. We observe that the PD increases marginally from epoch IX1 to epoch IX2 and subsequently drops in epoch IX3 as luminosity decreases $(1.68–0.35) \times 10^{37}$ erg s^{-1} (Figure 2(c)) and $F_{\rm BB}/F_{\rm PL}$ increases in the respective energy bands. Note that `bbodyrad` dominates $(1.5 \lesssim F_{\rm BB}/F_{\rm PL} \lesssim 3.4)$ in the 5–8 keV band, whereas `cutoffpl` becomes prominent $(0.4 \lesssim F_{\rm BB}/F_{\rm PL} \lesssim 1)$ in the 2–5 keV energy range. We observe that the PD reaches up to ∼3.0%–4.8% in 5–8 keV for which `bbodyrad` flux exceeds twice that of `cutoffpl`. However, it is important to note that the change in PD over the epochs in different energy bands is marginally significant at 74% (2–5 keV) and 73% (5–8 keV) confidence levels, respectively (see Table 2). Therefore, the results of the correlation study presented here need to be interpreted with caution considering their statistical significance.

3.3. Phase-resolved Polarimetric Properties

We search for pulsation using epoch-folding (Leahy et al. 1983) in the $2-8$ keV *IXPE* band, as well as in different energy bands (3–10, 10–20, 20–40, and 40–78 keV) of NuSTAR data. The pulse profiles are normalized by dividing with the average intensity of the respective energy bands. Uncertainties in the pulse periods were determined by producing simulated light curves at each epoch, and computing the rms variation in their determined periods (Leahy 1987; see also Chatterjee et al. 2021).

The source exhibits strong pulsations in all NuSTAR energy bands as well as in the entire energy band with $P = 9.79909$ (4) s. The pulse profiles and pulse fractions (PFs) are found to be strongly energy dependent as PF increases from ∼27% to ∼50% with the increase in energy (see Beri et al. 2021). The pulse profiles are dominated by emission from a single peak at lower energies and changes to a double-peaked profile at higher energies (R. Chatterjee et al. 2024, in preparation). Pulsations are also detected in all the IXPE epochs (see Table 2) in 2–8 keV with pulse profiles of a single-peaked (IX1, PF ∼ 18%), double-peaked (IX2, fundamental PF ∼ 15%), and triple-peaked (IX3, fundamental PF ∼ 10%) nature, respectively, with decreasing luminosity. The pulse profiles obtained with NuSTAR and IXPE are shown in panels (a) and (b) of Figure 5, respectively.

To investigate the phase-resolved polarization properties of Swift J0243.6+6124, we divide the epoch IX1 observation into five equal phase-bins of width 0.2 each and compute PD and PA in each bin, depicted in panels (b) and (c) of Figure 5, respectively. We observe a moderate variation of PD with phase in the range ∼1.7%–3.1%, exhibiting a possible correlation with intensity (see Figure 5(b)). Similarly, PA also shows marginal variation within 12°.2–25°.5 in the phase bins. In particular, we find that the variations of both PD and PA over different phase bins for IX1 are significant at 95.3% and 98.8% confidence levels against the phase-averaged values of the 2–8 keV energy range (see Table 2). However, we observe that the PD obtained in some phase bins remains close to or below the MDP$_{99}$% level, mainly due to limited statistics across the phase bins.[5] In Figure 3(c), we illustrate the variation of normalized Stokes parameters in multiple phase bins for epoch IX1. Following the approach mentioned in Section 3.2.1, we estimate the significance of the variation of the normalized Stokes parameters (Q/I and U/I) over five phase bins as 98.3% for epoch IX1. Indeed, the variation of the polarimetric properties of the source remains more significant ($>2\sigma$) in Stokes parameter space as compared to the variation in PD ($<2\sigma$), as explained earlier.

3.4. Broadband Spectral Distribution

We examine broadband (0.6–70 keV) energy spectral energy distribution of Swift J0243.6+6124 using quasi-simultaneous NICER (NI0) and NuSTAR (NU0) observations. In general, accretion-powered pulsars exhibit emission over a wide range of energies, including soft X-ray peaks and hard tails at higher energies. We adopt a model combination `const*Tbabs*(Gaussian+bbodyrad+cutoffpl)` comprising a `bbodyrad` component for thermal emission along with a `cutoffpl`, accounted for higher energy cut-off, to model the broadband continuum. The `Gaussian` is used to model the strong iron line emission observed at ∼6.4 keV, and `Tbabs` (Wilms et al. 2000) takes care of the interstellar absorption. We find the best fit with the above model combination as $\chi^2_{\rm red}(\chi^2/d.o.f) = 1.13$ (3136/2765). Further, we model the NICER spectra during epochs NI1, NI2, and NI3 in the 0.6–11 keV energy range. Note that a similar model combination provides an acceptable fit for all NICER spectra with $0.91 \leqslant \chi^2_{\rm red} \leqslant 1.06$.

The best-fitted broadband spectrum (NI0+NU0) results in seed photon temperature $kT_{\rm bb} = 0.86 \pm 0.03$ keV with norm$_{\rm bbody}$= 135^{+24}_{-20}. We find the photon index (Γ) of `cutoffpl` as 0.98 ± 0.01 with a high energy cut-off ($E_{\rm c}$) at 20.16 ± 0.24 keV. The hydrogen column density ($n_{\rm H}$) is found to be $(1.01 \pm 0.01) \times 10^{22}$ cm^{-2}. We detect iron line emission at 6.45 ± 0.02 keV of line width 0.24 ± 0.03 keV in NI0+NU0. In addition, $kT_{\rm bb} = 3.50^{+0.61}_{-0.34} - 3.92^{+0.16}_{-0.15}$ keV, norm$_{\rm bbody} = 2.26^{+1.07}_{-0.97} - 5.25^{+0.64}_{-0.59}$, and $\Gamma = 0.57^{+0.11}_{-0.10} - 1.08^{+0.02}_{-0.02}$ are obtained during NI1–NI3 observations. Note that $E_{\rm c}$ remains unconstrained in the NICER spectra of NI1–NI3, and hence we freeze it at 6 keV.

Using `cflux`, we obtain the bolometric flux (0.1–100 keV) as 3.57×10^{-8} erg cm^{-2} s^{-1} in NI0+NU0, which decreases sharply in the range $(2.75–0.72) \times 10^{-8}$ erg cm^{-2} s^{-1} during NI1 to NI3. Considering a distance of 6.8 kpc to the source (Bailer-Jones et al. 2018), we find the bolometric luminosity of the source as 1.98×10^{38} erg s^{-1} for NI0+NU0, which exceeds the Eddington limit of XRPs, confirming its ultraluminous nature (see also Wilson-Hodge et al. 2018; Chhotaray et al. 2024). In Figure 6, we show the best-fitted broadband (0.6–70 keV) energy spectrum of combined NI0+NU0 observations along with NICER spectra (0.6–11 keV) during NI1–NI3 epochs. The dotted lines of various colors depict the best-fitted `bbodyrad` component corresponding to the respective spectra. It is worth noting that despite NI0 and NI1 observations being roughly a month apart, the spectral shapes appear to remain quite similar (see Figures 1 and 6).

4. Discussion

In this Letter, we report the results of spectropolarimetric studies of the Galactic ULXP Swift J0243.6+6124 using the first-ever IXPE observations (2–8 keV) during the 2023 outburst. We carry out an epoch-dependent spectropolarimetric study with IXPE over three epochs (IX1, IX2, and IX3) with an integrated exposure of ∼375 ks.

[5] More than five phase bins are avoided as the PD remains below the MDP$_{99}$% level. See the Appendix for details.

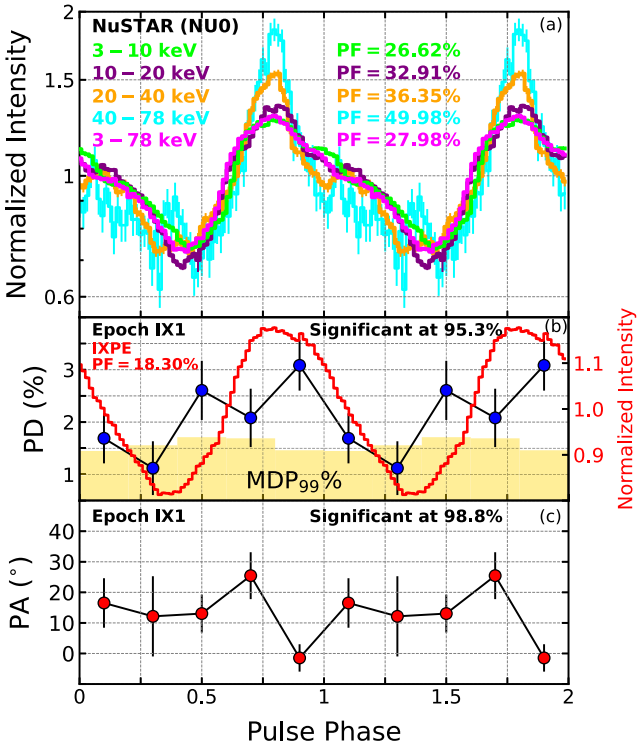

Figure 5. Panel (a): pulse profile of Swift J0243.6+6124 obtained from NuSTAR in different energy bands are depicted with different colors. Panel (b): variation of PD and pulse profile with the pulse phase (2–8 keV) for epoch IX1. Histograms denote MDP_{99}%. Panel(c): variation of PA with pulse phase for epoch IX1. Note that the variations of PD and PA over different phase bins are marginal. See the main text for details.

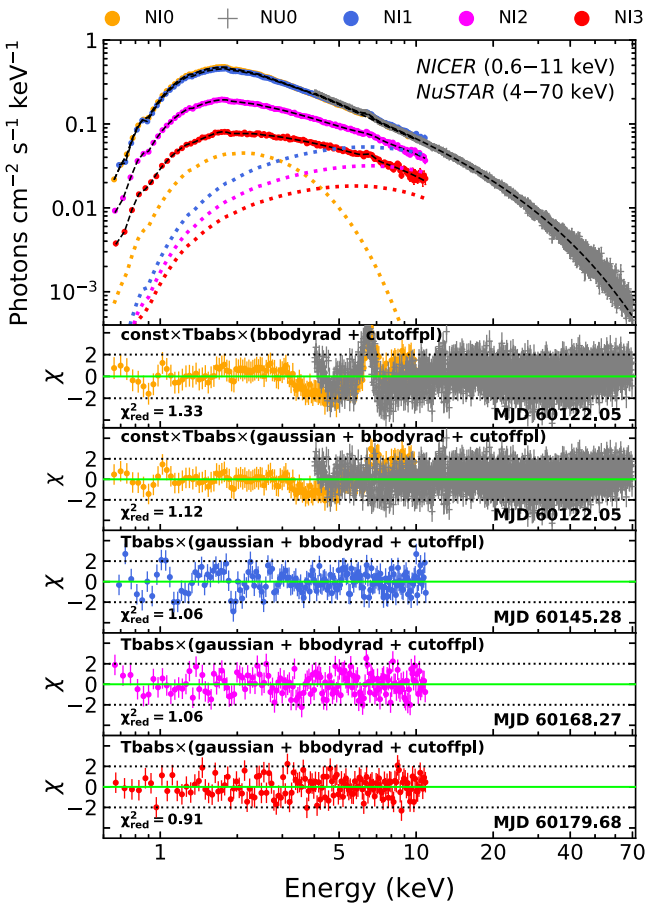

Figure 6. Best-fitted broadband energy spectra of Swift J0243.6+6124 in the 0.6–70 keV energy band from quasi-simultaneous NICER and NuSTAR observations (NI0 and NU0) and NICER spectra (0.6–11 keV) during epoch NI1, NI2, and NI3, respectively. See the main text for details.

Indeed, the main findings obtained in this work is the detection of significant polarized emission of PD $\sim 2.0\% \pm 0.2\%$ ($>8\sigma$) and PA $\sim 10\overset{\circ}{.}8 \pm 3\overset{\circ}{.}3$ in the 2–8 keV energy range during epoch IX1. This finding confirms Swift J0243.6+6124 as the first ULXP that exhibits the signature of polarized emissions. We find that the PD increases up to $\sim$3.1% in epoch IX2 and eventually decreases to $\sim$2.4% during epoch IX3. However, moderate variation of PD with energy reaching up to $\sim$3.3% (IX1), $\sim$4.5% (IX2), and $\sim$3.6% (IX3) at $\sim$7 keV (see Figure 2(b) and Table 2) is observed. Notably, no significant variation of PA is seen in different energy ranges for all the epochs. Needless to mention that the observed PD appears much lower compared to the theoretical model predictions (up to $\sim$80%) for XRPs (Meszaros et al. 1988; Caiazzo & Heyl 2021a, 2021b). Owing to that, the polarization results of Swift J0243.6+6124 are in agreement with the reported "low" PDs in other XRPs, namely Cen X−1 ($\sim$5.8%; Tsygankov et al. 2022), 4U 1626−67 (<4%; Marshall et al. 2022), and Vela X−1 ($\sim$2.3%; Forsblom et al. 2023).

We also find that the PD increases with the decrease in luminosity between epoch IX1 and IX2 (Figure 2(c)) and subsequently decreases at epoch IX3. Intriguingly, we observe an overall increase of PD as 3%–4.8% in the presence of a dominant `bbodyrad` emission ($1.5 \lesssim F_{\rm BB}/F_{\rm PL} \lesssim 3.4$) at higher energies ($\gtrsim$5 keV) of the IXPE spectra. Nevertheless, PD remains within 1.65%–2.42% in `cutoffpl` dominated spectral domain ($0.4 \lesssim F_{\rm BB}/F_{\rm PL} \lesssim 1$) below $\sim$5 keV (see Figure 2(c)). In addition, the spectra of quasi-simultaneous NICER epochs (NI1, NI2, and NI3) also show the dominance of the `bbodyrad` component beyond $\sim$5 keV (see Figure 6). Based on these findings, we infer that the `bbodyrad` emission contributes to the observed high polarization degree up to $\sim$7 keV, and the `cutoffpl` component (dominated in $\sim$2–5 keV) results in a depolarization in the 2–8 keV energy band with PD $\sim$2%–3.1%.

We detect strong pulsations in Swift J0243.6+6124 with a spin period of $\sim$9.79 s (see Serim et al. 2023; Chhotaray et al. 2024) during epoch IX1 in the 2–8 keV energy range with a PF of $\sim$18% (Figure 5(b)). NuSTAR also detects a $\sim$9.79 s pulsation period (3–78 keV) with PF $\sim$28%. The energy-dependent pulsation study with NuSTAR further yields a monotonic increase of PF from 27% (3–10 keV) to 50% (40–78 keV). The phase-resolved polarimetric study reveals the variation of PD and PA within $\sim$1.7%–3.1% and $\sim 12\overset{\circ}{.}2$–$25\overset{\circ}{.}5$ with pulse phase, respectively. Interestingly, we observe a marginal correlation between PD and the pulse intensity with a minimal variation of PA (see Figure 5(c)). However, an anticorrelation between PD and source intensity is reported for several XRPs including Cen X−3 (Tsygankov et al. 2022) and GRO J1008−57 (Tsygankov et al. 2023). It is worth mentioning that, unlike the case of Swift J0243.6+6124, several pulsars exhibit relatively high PD ($\gtrsim$10%) along with significant PA variation as reported from phase-dependent polarimetric studies (Tsygankov et al. 2022; Forsblom et al. 2023; Suleimanov et al. 2023; Tsygankov et al. 2023). Moreover, the wide variation of PA over phase bins in many

such pulsars is satisfactorily described using the rotating vector model (Radhakrishnan & Cooke 1969; Poutanen 2020).

Meanwhile, various physical mechanisms are proposed to explain the relatively "low" PDs observed in most of the XRPs. These include (a) a reflected fraction of hot spot emission from the NS surface, (b) an accretion curtain, and (c) an accretion disk, all of which have the potential to produce substantial polarization (Tsygankov et al. 2022) depending on the magnetic field strength of the NS atmosphere (Poutanen et al. 1996). In addition, the emissions reflected from the optical companion can alter the polarization state depending on the pulsar's beam pattern (Tsygankov et al. 2022). However, this effect becomes significant only above $\sim$10 keV, making its contribution negligible in the IXPE band. The pronounced variation of the PA with pulse phases leads to seemingly "low" averaged PDs, despite significant polarization being evident in phase-dependent estimates (Suleimanov et al. 2023).

Alternatively, it is proposed that "vacuum resonance" at the transition point between the overheated upper NS surface and the relatively cooler underlying layer could play a viable role (Doroshenko et al. 2022). In particular, ordinary and extraordinary modes of polarization start to convert into each other while passing through the vacuum resonance, where the polarization contribution from plasma and vacuum birefringence becomes equal (Lai & Ho 2002). In other words, these two contributions acting against each other result in the depolarization of radiation. Note that this effect may be enhanced for the XRPs at critical luminosity with variations in the emission regions (Doroshenko et al. 2022; Tsygankov et al. 2022). Swift J0243.6+6124 with $\sim 10^{13}$ G surface magnetic field (Kong et al. 2022) exhibits critical luminosity $\gtrsim 10^{37}$ erg s^{-1} (Mushtukov et al. 2015), which is close to the estimated luminosities during the IXPE campaign. Hence, we speculate that the observed "low" PD in Swift J0243.6+6124 possibly resulted because of the vacuum resonance similar to the predictions for Her X−1 (Doroshenko et al. 2022) and Cen X−1 (Tsygankov et al. 2022). However, the possibility of explaining the observed "low" PD using alternative physical mechanisms cannot be entirely ruled out.

The broadband energy spectrum (0.6–70 keV) with NICER and NuSTAR during NI0+NU0, described by `bbodyrad` and `cutoffpl` components, indicates bolometric luminosity (0.1–100 keV) as 1.98×10^{38} erg s^{-1}. The bolometric luminosity is seen to decrease as $1.52–0.40 \times 10^{38}$ erg s^{-1} in the NICER epochs (NI1, NI2, and NI3) during the decay phase of the outburst. A substantially higher luminosity of approximately $\sim 40 L_{\rm Edd}$ was observed during the source's 2017 outburst, confirming its ultraluminous nature (Tsygankov et al. 2018).

In conclusion, we report the first detection of phase-averaged as well as phase-resolved polarization in the Galactic X-ray pulsar Swift J0243.6+6124 during the decaying phase of the 2023 outburst.

Acknowledgments

The authors thank the anonymous reviewer for constructive comments and useful suggestions that helped to improve the quality of the manuscript. S.D. thanks Science and Engineering Research Board (SERB) of India for support under grant MTR/2020/000331. R.C., K.J., and A.N. thank GH, SAG, DD, PDMSA, and Director, URSC for encouragement and continuous support to carry out this research. This publication uses data from the IXPE, NICER, and NuSTAR missions. This research has made use of the MAXI data provided by RIKEN, JAXA, and the MAXI team (Matsuoka et al. 2009). The Swift/BAT transient monitor results provided by the Swift/BAT team are also used (Krimm et al. 2013). We thank each instrument team for processing the data and providing the necessary software tools for the analysis.

Data Availability

Data used for this publication are currently available at the HEASARC browse website (https://heasarc.gsfc.nasa.gov/db-perl/W3Browse/w3browse.pl).

Appendix
Pulse-phase-dependent Analysis

To investigate the finer phase variations of the polarimetric properties of Swift J0243.6+6124, we repeat our phase-resolved polarimetric analysis considering a higher number of phase bins for epoch IX1. Barycentric correction as well as correction for the binary orbit of the source using its orbital parameters[6] (Malacaria et al. 2020) are applied to the events. We divide the data of the 3–8 keV energy band into 24 phase bins following the recent analysis by Poutanen et al. (2024), which is related to the present Letter. The obtained results are depicted in Figure A1, where we present the variation of normalized intensity, normalized Stokes parameters (Q/I and U/I), PD, and PA in panels (a)–(e), respectively. We observe moderate variation in Q/I and U/I, significant at 98.8% and 94% confidence levels, respectively, over the phase bins. The PD is found to vary in the range of $\sim$1%–5.5%, significant at an 83% confidence level, although remaining below the MDP_{99}% level in most of the phase bins (see panel (d)). This could occur as a result of insufficient photon statistics within the respective phase bins. Furthermore, we observe a noticeable variation of PA as $-68^\circ \lesssim \mathrm{PA} \lesssim 65^\circ$ over different phase bins of the IX1 epoch. It is worth mentioning that as the PD measurements are below the MDP_{99}% level, the corresponding PA variations deserve careful consideration.

[6] https://gammaray.nsstc.nasa.gov/gbm/science/pulsars/lightcurves/swiftj0243.html

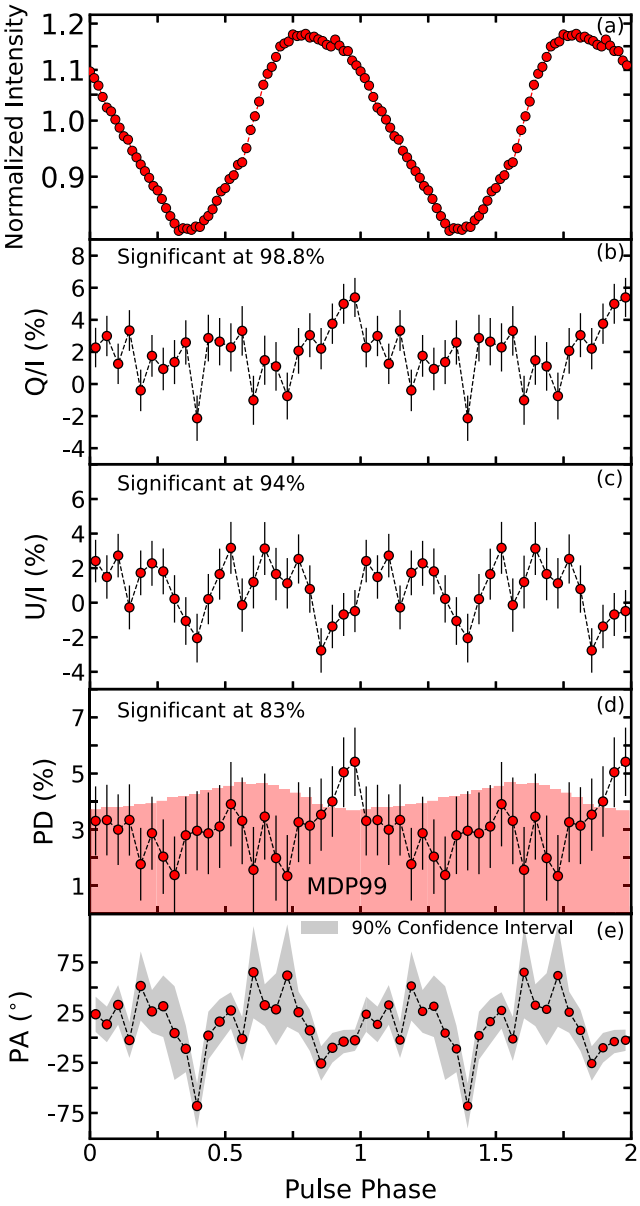

Figure A1. Phase-resolved polarimetric analysis of Swift J0243.6+6124 during epoch IX1 in the 3–8 keV energy range over 24 phase bins. In panels (a)–(e), variations of normalized intensity, normalized Stokes parameters (Q/I and U/I), PD, and PA with pulse phase are shown. In panel (d), the histograms denote the MDP_{99}% level. In panel (e), the gray shaded area represents 90% confidence intervals. See the main text for details.

ORCID iDs

Seshadri Majumder https://orcid.org/0000-0002-2214-35937
Kiran M. Jayasurya https://orcid.org/0000-0002-3430-9837
Santabrata Das https://orcid.org/0000-0003-4399-5047

References

Atapin, K., Fabrika, S., & Caballero-García, M. D. 2019, MNRAS, 486, 2766
Bachetti, M., Harrison, F. A., Walton, D. J., et al. 2014, Natur, 514, 202
Bailer-Jones, C. A. L., Rybizki, J., Fouesneau, M., Mantelet, G., & Andrae, R. 2018, AJ, 156, 58
Baldini, L., Bucciantini, N., Lalla, N. D., et al. 2022, SoftX, 19, 101194
Basko, M. M., & Sunyaev, R. A. 1976, MNRAS, 175, 395
Beri, A., Naik, S., Singh, K. P., et al. 2021, MNRAS, 500, 565
Caiazzo, I., & Heyl, J. 2021a, MNRAS, 501, 129
Caiazzo, I., & Heyl, J. 2021b, MNRAS, 501, 109
Chatterjee, R., Agrawal, V. K., & Nandi, A. 2021, MNRAS, 505, 3785
Chhotaray, B., Jaisawal, G. K., Nandi, P., et al. 2024, ApJ, 963, 132
Doroshenko, V., Poutanen, J., Tsygankov, S. S., et al. 2022, NatAs, 6, 1433
Feng, H., & Soria, R. 2011, NewAR, 55, 166
Forsblom, S. V., Poutanen, J., Tsygankov, S. S., et al. 2023, ApJL, 947, L20
Goodman, J., & Weare, J. 2010, CAMCS, 5, 65
Jayasurya, K. M., Agrawal, V. K., & Chatterjee, R. 2023, MNRAS, 525, 4657
Kennea, J. A., Lien, A. Y., Krimm, H. A., Cenko, S. B., & Siegel, M. H. 2017, ATel, 10809, 1
King, A., Lasota, J.-P., & Middleton, M. 2023, NewAR, 96, 101672
Kislat, F., Clark, B., Beilicke, M., & Krawczynski, H. 2015, APh, 68, 45
Kong, L.-D., Zhang, S., Zhang, S.-N., et al. 2022, ApJL, 933, L3
Krawczynski, H., Muleri, F., Dovčiak, M., et al. 2022, Sci, 378, 650
Krimm, H. A., Holland, S. T., Corbet, R. H. D., et al. 2013, ApJS, 209, 14
Kushwaha, A., Jayasurya, K. M., Agrawal, V. K., & Nandi, A. 2023, MNRAS, 524, L15
Lai, D., & Ho, W. C. G. 2002, ApJ, 566, 373
Leahy, D. A. 1987, A&A, 180, 275
Leahy, D. A., Darbro, W., Elsner, R. F., et al. 1983, ApJ, 266, 160
Majumder, S., Das, S., Agrawal, V. K., & Nandi, A. 2023, MNRAS, 526, 2086
Majumder, S., Kushwaha, A., Das, S., & Nandi, A. 2024, MNRAS, 527, L76
Malacaria, C., Jenke, P., Roberts, O. J., et al. 2020, ApJ, 896, 90
Malacaria, C., Heyl, J., Doroshenko, V., et al. 2023, A&A, 675, A29
Marshall, H. L., Ng, M., Rogantini, D., et al. 2022, ApJ, 940, 70
Matsuoka, M., Kawasaki, K., Ueno, S., et al. 2009, PASJ, 61, 999
Meszaros, P., Novick, R., Szentgyorgyi, A., Chanan, G. A., & Weisskopf, M. C. 1988, ApJ, 324, 1056
Mushtukov, A., & Tsygankov, S. 2022, arXiv:2204.14185
Mushtukov, A. A., Suleimanov, V. F., Tsygankov, S. S., & Poutanen, J. 2015, MNRAS, 447, 1847
Mushtukov, A. A., Tsygankov, S. S., Poutanen, J., et al. 2023, MNRAS, 524, 2004
Poutanen, J. 2020, A&A, 641, A166
Poutanen, J., Nagendra, K. N., & Svensson, R. 1996, MNRAS, 283, 892
Poutanen, J., Tsygankov, S. S., Doroshenko, V., et al. 2024, arXiv:2405.08107
Radhakrishnan, V., & Cooke, D. J. 1969, ApL, 3, 225
Reig, P., Fabregat, J., & Alfonso-Garzón, J. 2020, A&A, 640, A35
Serim, M. M., Dönmez, Ç. K., Serim, D., et al. 2023, MNRAS, 522, 6115
Strohmayer, T. E. 2017, ApJ, 838, 72
Suleimanov, V. F., Forsblom, S. V., Tsygankov, S. S., et al. 2023, A&A, 678, A119
Tsygankov, S. S., Doroshenko, V., Mushtukov, A. A., Lutovinov, A. A., & Poutanen, J. 2018, MNRAS, 479, L134
Tsygankov, S. S., Doroshenko, V., Poutanen, J., et al. 2022, ApJL, 941, L14
Tsygankov, S. S., Doroshenko, V., Mushtukov, A. A., et al. 2023, A&A, 675, A48
Walton, D. J., Fürst, F., Heida, M., et al. 2018, ApJ, 856, 128
Weisskopf, M. C., Soffitta, P., Baldini, L., et al. 2022, JATIS, 8, 026002
Wilms, J., Allen, A., & McCray, R. 2000, ApJ, 542, 914
Wilson-Hodge, C. A., Malacaria, C., Jenke, P. A., et al. 2018, ApJ, 863, 9